communications physics

ARTICLE

https://doi.org/10.1038/s42005-021-00677-2 OPEN

Efficient harmonic generation in an adiabatic multimode submicron tapered optical fiber

Chang Kyun Ha[1], Kee Hwan Nam[1] & Myeong Soo Kang[1✉]

Optical nanotapers fabricated by tapering optical fibers have attracted considerable interest as an ultimate platform for high-efficiency light-matter interactions. While previously demonstrated applications relied exclusively on the low-loss transmission of only the fundamental mode, the implementation of multimode tapers that adiabatically transmit several modes has remained very challenging, hindering their use in various emerging applications in multimode nonlinear optics and quantum optics. Here, we report the realization of multimode submicron tapers that permit the simultaneous adiabatic transmission of multiple higher-order modes including the LP_{02} mode, through introducing deep wet-etching of conventional fiber before fiber tapering. Furthermore, as a critical application, we demonstrate fundamental-to-fundamental all-fiber third-harmonic generation with high conversion efficiencies. Our work paves the way for ultrahigh-efficiency multimode nonlinear and quantum optics, facilitating nonclassical light generation in the multimode regime, multimode soliton interactions and photonic quantum gates, and manipulation of the evanescent-field-induced optical trapping potentials of atoms and nanoparticles.

[1] Department of Physics, Korea Advanced Institute of Science and Technology (KAIST), Daejeon, Republic of Korea. ✉email: mskang@kaist.ac.kr

Optical micro/nanotapers (OMNTs), which can guide light along the subwavelength-diameter waist[1,2], have been utilized as a versatile photonic platform in a vast range of applications. The significant evanescent field can be exploited to achieve near-unity-efficiency evanescent light coupling to other photonic systems[3–6], tight optical trapping of atoms[7–10] and nanoparticles[11,12] in the vicinity of the waist for their efficient interactions with the guided light, as well as high-sensitivity optical detection of gases and chemicals[13,14]. Various nonlinear and quantum optical phenomena in OMNTs have also attracted growing interest. OMNTs provide not only tight confinement of light within a tiny cross-section, which yields radically enhanced effective optical nonlinearities, but also a unique capability of simple and broad dispersion engineering through varying the waist thickness. These properties have enabled broader-than-octave-spanning supercontinuum generation[15], optical excitation of strongly confined coherent acoustic phonons[16,17], and creation of correlated photon pairs via spontaneous four-wave mixing[18,19].

While these experiments were demonstrated using the light guided in the fundamental LP_{01} mode only, several emerging applications can be facilitated exclusively by utilizing the higher-order modes (HOMs), as they allow access to substantially broad landscapes of optical dispersion for intermodal phase-matching of multimode nonlinear and quantum optical processes and engineering of the evanescent field patterns for controlling the spatial profiles of optical trapping potentials. For instance, high-efficiency nonlinear optical frequency conversion processes such as harmonic generation[20–25] and parametric down-conversion (i.e., the inverse process of the harmonic generation)[26,27] in OMNTs demand phase-matching between the fundamental wave in the LP_{01} mode and the harmonic in the HOM[28]. Photon-pair generation via intermodal four-wave mixing[29] and multimode soliton dynamics such as single-pump optical event horizon interactions[30] and soliton self-mode conversion[31] have also been recently proposed as novel intermodal nonlinear effects involving the HOMs. They may be implemented at very low pump powers or with shorter interaction lengths in the highly nonlinear OMNT platform, compared to the conventional multimode fiber counterparts.

All these applications require high-purity coupling and low-loss robust transmission of multiple HOMs, particularly the LP_{0m} modes ($m > 1$) having the same azimuthal dependence of the field distribution as the LP_{01} mode, in OMNTs. However, such multimode OMNTs have not been successfully demonstrated so far, and their realization has long remained a major challenge. Some recent experimental demonstrations have been limited to two-mode OMNTs that adiabatically transmit the LP_{01} and the LP_{11} modes only, relying on the use of specially designed fiber with a reduced cladding[32,33] or an unconventional index distribution[34,35].

In this paper, we report the realization of multimode adiabatic submicron tapers (MASTs) that permit the simultaneous adiabatic transmission of the LP_{02} mode together with the LP_{01}, the LP_{11}, and the LP_{21} modes. In contrast to the popular method of direct tapering of optical fiber, we employ a two-step process: deep wet-etching a section of optical fiber to a carefully predetermined cladding diameter below ~20 μm and tapering the etched fiber down to a targeted submicron waist diameter. Our fabrication method works even with commercial off-the-shelf step-index fiber, offering excellent compatibility with standard fiber-optic systems, and does not rely on the use of specially designed fibers. Furthermore, as an immediate and critical application of the MAST, we also demonstrate the fundamental-to-fundamental all-fiber third-harmonic generation (THG) with high conversion efficiencies $>10^{-4}$, which was theoretically studied in a couple of proposals[28,36] but has been far from successful yet. This process is a highly efficient means of generating high-beam-quality coherent light in the visible and ultraviolet spectra in the fiber platform. Moreover, it is the very prerequisite for realizing the exact reverse, the fundamental-to-fundamental third-order parametric down-conversion[26,27], which has received considerable attention as a new type of nonclassical light source, although this is yet to be experimentally demonstrated.

Results

Multimode adiabatic submicron taper (MAST). Figure 1 describes the operating principle and numerical design of a silica MAST. Silica OMNTs can be fabricated by heating and pulling a section of unjacketed silica optical fiber[37], which creates a pair of transition regions connecting the taper waist and intact optical fiber. For the adiabatic guidance of an optical mode along the OMNT, the effective index of the mode should be kept sufficiently distinct from those of the other modes in the transition region[37,38]. However, an ultimate limitation in implementing MASTs with tapering conventional optical fiber is that HOMs become very close to each other in terms of effective index right after they are transformed into the cladding modes at the taper transition. Figure 1a shows the calculated effective indices of several optical modes at 532 nm wavelength over a range of taper diameter in the case when a section of 125-μm-thick optical fiber is tapered. The HE_{11} (LP_{01}) mode is well isolated from all HOMs. As a result, it transmits adiabatically through the taper at any diameter for ordinary (i.e., not too steep) taper transitions[37]. In sharp contrast, the effective indices of the HOMs get very similar to each other when they are guided as the cladding modes near the core-mode cutoff diameter. The inset in Fig. 1a highlights the case of three hybrid HOMs of our primary interest in this work—the EH_{11} and the HE_{31} modes (belonging to LP_{21}), and the HE_{12} (LP_{02}) mode. The HE_{12} mode becomes almost degenerate with both the EH_{11} and the HE_{31} modes around the taper diameter of 71.6 μm. It should be noted that the EH_{11} and the HE_{12} modes exhibit anti-crossing, their intermodal beatlength markedly larger than 1 m as shown in Fig. 1b. Furthermore, these modes closely approach the EH_{12} and the HE_{13} modes that are already cladding-guided in the intact (non-tapered) fiber. The EH_{11} and the HE_{12} modes display another anti-crossing at the taper thickness of 11.8 μm, where the core becomes so thin that its role in the light guidance becomes negligible. Such complicated structures of modal anti-crossing, as well as crossing, emerge for many pairs of hybrid HOMs, in particular for the $EH_{l,m}$ (belonging to $LP_{l+1,m}$) and the $HE_{l,m+1}$ (belonging to $LP_{l-1,m+1}$) modes (l, m: positive integers), at specific taper diameters, which hinders their low-loss adiabatic transmission.

We overcome this bottleneck by significantly reducing the initial cladding diameter before the tapering process. Figure 1c displays the calculated effective indices in the scenario when the cladding diameter is decreased to 17 μm prior to tapering, while leaving the initial core parameters unchanged. The near-degeneracy among the cladding-guided HOMs is strongly lifted, and as a result, each mode is well separated from other modes at any taper diameter. In particular, the anti-crossing of the EH_{11} and the HE_{12} modes disappears, and the intermodal beatlength between the two modes decreases to a few millimeters or below any taper diameters (Fig. 1d), which is sufficient for the adiabatic transmission of both modes. We examine the criterion on the initial cladding diameter desirable for the adiabatic transmission of the HOMs. The maximum intermodal beatlength between the EH_{11} and the HE_{12} mode over the entire range of possible taper diameter is obtained as a function of the initial cladding diameter, as shown in Fig. 1e. This result indicates that the fiber cladding should be deeply etched below ~20 μm thickness (roughly twice the core diameter) for the adiabatic transmission of the two

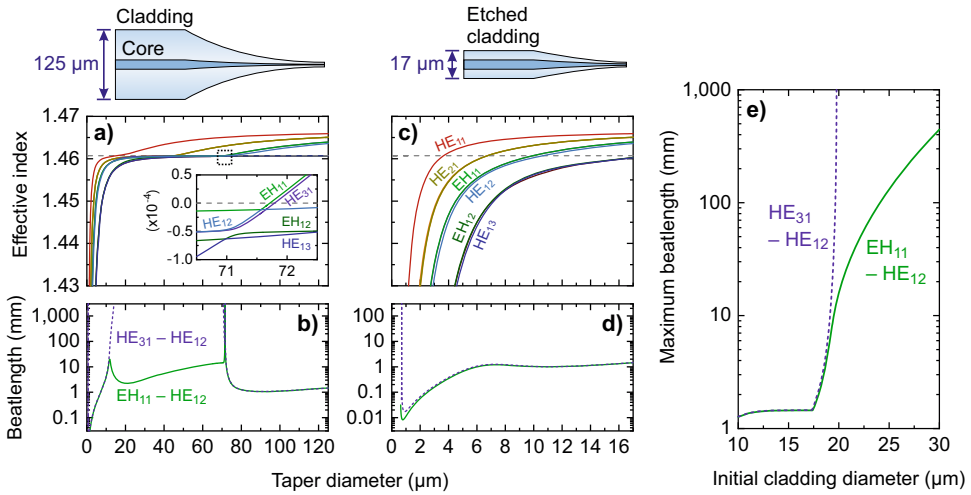

Fig. 1 Operating principle and numerical design of multimode adiabatic submicron taper. a Calculated effective indices of several optical modes over a range of taper diameter in the case when a 125-μm-thick conventional step-index silica optical fiber (core diameter: 8.7 μm, numerical aperture: 0.13) is directly tapered. The inset is the zoomed-in plot around the black dotted box, where the vertical axis represents the relative effective index from the refractive index of fused silica cladding (gray horizontal dashed lines in (**a**) and (**c**)). It can be seen that the anti-crossing of the EH_{11} (light green) and the HE_{12} (light blue) modes appears as they are transformed from the core modes to the cladding modes. Such an anti-crossing also takes place between the EH_{12} (dark green) and the HE_{13} (dark blue) modes, which are already the cladding modes in the intact (non-tapered) fiber. **b** Intermodal beatlength between the EH_{11} and the HE_{12} mode (green solid curve) and that between the HE_{31} and the HE_{12} mode (violet dotted curve) obtained from **a**. **c** Calculated effective indices over a range of taper diameter in the scenario when a 17-μm-thick cladding-etched fiber is tapered. **d** Intermodal beatlength between the EH_{11} and the HE_{12} mode (green solid curve) and that between the HE_{31} and the HE_{12} mode (violet dotted curve) obtained from **c**. **e** Maximum intermodal beatlength between the EH_{11} and the HE_{12} mode (green solid curve) and that between the HE_{31} and the HE_{12} mode (violet dotted curve) during the tapering process as a function of the initial diameter of etched cladding. All calculations are performed at 532 nm wavelength. In **a** and **c**, the TE_{01} and the TM_{01} modes are almost degenerate with the HE_{21} mode, implying that they cannot be distinguished from each other in the effective index scale. Similarly, the EH_{11} and the HE_{31} modes are almost degenerate and thus not distinct from each other.

modes, where the intermodal beatlength is maintained below ~10 mm during the entire tapering process. We also consider the possibility of the coupling between the HE_{12} and the HE_{31} mode at their crossing points, as shown in Fig. 1. Their coupling is forbidden in an idealized taper having a perfect circular symmetry in the taper cross-section owing to the orthogonality between the azimuthal dependences of the two modes. However, the circular symmetry of the taper cross-section can be easily broken in reality due to the unavoidable imperfection of the tapering process, such as the gas flow, fiber sagging, and flame instability. Then, the two modes can experience intermodal coupling at their crossing points, which would disturb their adiabatic transmission. Nevertheless, in the case of tapering etched fiber, it turns out that the intermodal beatlength between the two modes is also significantly reduced and maintained at a few millimeters or below until the mode-crossing waist diameter (0.7 μm) near their cutoff is reached, as can be seen in Fig. 1d.

Based on this operating principle, we fabricate silica MASTs employing a two-step process, as described in Fig. 2 (see "Methods"). We produce MASTs having a waist length of 10 mm and an exponentially shaped transition at both ends of the waist. The length of each taper transition is estimated to be ~60 mm when the waist diameter reaches 0.76 μm. The transmission and the output far-field pattern are recorded for each input HOM during the entire tapering process, as illustrated in Fig. 3a (see "Methods"). Until the waist diameter reaches ~0.9 μm, the transmission is maintained above 93% for any input HOM, as shown in Fig. 3b–d. It is repeatedly seen in this process that the transmission first decreases continuously until the waist diameter is reduced to 6–8 μm, and after that, it gradually recovers. This trend is associated with our observation that the heated fiber section first sags slightly under its weight, and it becomes straight back as the waist diameter decreases below 6–8 μm, as getting lighter and more affected by the upward butane–oxygen flow in our current tapering facility. When the waist diameter is further reduced below ~0.9 μm, the transmission drops slightly to ~85%. This degradation is attributed to the fact that the taper becomes rather lifted and curved under the influence of butane–oxygen flow, which lowers the thickness uniformity of the taper waist[33,39]. Nevertheless, during the entire tapering process, the far-field pattern of the output beam is not significantly distorted. For the LP_{02} mode (Fig. 3b), in particular, the output far-field pattern is almost unchanged until the mode eventually becomes cut off. For comparison, we repeat the in situ characterization of the LP_{02} mode transmission, fabricating nanotapers using the conventional approach of direct tapering of 125-μm-thick optical fiber without cladding etching (corresponding to Fig. 1a, b). The severely degraded transmission and output far-field patterns displayed in Supplementary Fig. 1 and Supplementary Movie 1 reveal the nonadiabatic transmission of the LP_{02} mode in the conventional fiber tapers. On the other hand, the LP_{21} and the LP_{11} modes are not single vector eigenmodes but combinations of {the EH_{11} and HE_{31} modes} and {the TE_{01}, TM_{01}, and HE_{21} modes}, respectively, leading to the continuous change of the orientation and visibility of intensity lobes in the output field profile during the tapering process. (see Supplementary Movies 2 and 3 for the LP_{21} and the LP_{11} mode, respectively).

High-efficiency fundamental-to-fundamental all-fiber THG in MAST. The adiabatic transmission of the HOMs through a MAST is exclusively beneficial to several new applications. As an immediate and critical application of the MAST capable of robust transmission of the LP_{02} mode, we demonstrate the fundamental-to-fundamental all-fiber THG with high conversion efficiencies. It has been theoretically suggested that phase-matching between the fundamental wave in the HE_{11} mode and the third harmonic in

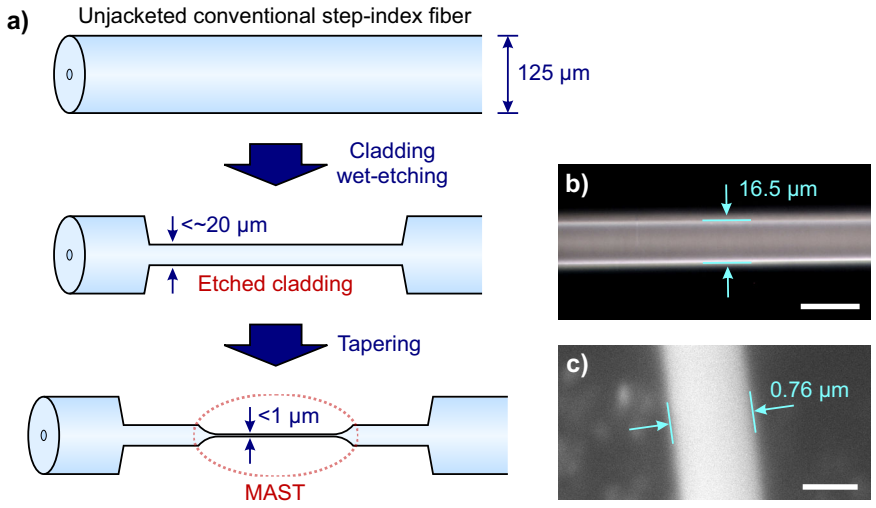

Fig. 2 Fabrication of multimode adiabatic submicron tapers (MASTs). a Fabrication process of a silica MAST. A section of unjacketed conventional step-index silica optical fiber is etched to a thickness below ~20 μm. The etched cladding is then tapered to a submicron thickness using the flame brushing and pulling technique[37]. **b** Optical micrograph of a 16.5-μm-thick cladding-etched fiber. The white scale bar corresponds to 20 μm. **c** Scanning electron micrograph of a 0.76-μm-thick silica MAST. The white scale bar corresponds to 500 nm.

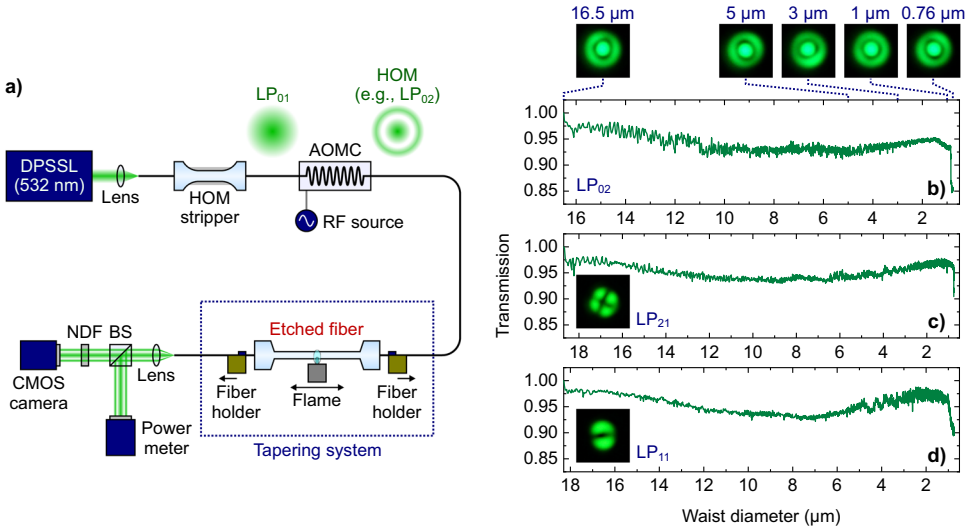

Fig. 3 In situ optical characterization of multimode adiabatic submicron tapers (MASTs) during the tapering process. a Schematic diagram of the experimental setup for the fabrication and in situ transmission measurement of a silica MAST. A higher-order mode (HOM) at 532 nm wavelength is generated through in-fiber acousto-optic mode conversion from the input LP_{01} mode and then launched into the tapering system. The transmission and output far-field pattern are monitored with a power meter and a complementary metal-oxide-semiconductor (CMOS) camera, respectively, during the tapering process. DPSSL diode-pumped solid-state laser, AOMC acousto-optic mode converter, RF radio frequency, BS 50/50 beam splitter, NDF neutral density filter. **b**–**d** Transmission and output far-field pattern that are recorded during the entire tapering process, when the LP_{02} mode (**b**), the LP_{21} mode (**c**), or the LP_{11} mode (**d**) is launched into the input port. In **c** and **d**, the CMOS images are the far-field patterns before the tapering process starts.

the HE_{12} mode provides the highest THG efficiencies in OMNTs[28]. In relevant previous experiments[20–22], however, the nonadiabatic transmission of the third-harmonic signal generated in the HE_{12} mode has seriously deteriorated the THG performance, such as the conversion efficiency and third-harmonic beam quality. Figure 4a illustrates our experimental scheme of all-fiber THG, where the input pump beam in the LP_{01} mode is eventually converted into the third harmonic in the LP_{01} mode. For efficient THG, the phase-matching condition should be satisfied, i.e., the effective indices of the fundamental wave and the third harmonic should be the same. We fabricate MASTs with a waist diameter of 0.76 μm (Fig. 2c), which is theoretically predicted to yield the phase-matched THG from the HE_{11} mode at 1551 nm wavelength to the HE_{12} mode at 517 nm[28]. (see Supplementary Note 1 and Supplementary Fig. 2 for details on the calculated phase-matching MAST waist diameter) The MAST is pumped by optical pulses generated from a master oscillator power amplifier (MOPA) system. The MOPA system employs our widely tunable ultra-narrow-linewidth erbium-doped soliton fiber laser[40] as the master oscillator. The pump beam is partly converted into the third harmonic in the HE_{12} mode in the MAST, which is then transformed into the desired LP_{01} mode at a home-made all-fiber acoustic-optic mode converter (AOMC)[41,42] right after the MAST (see "Methods" for more details on the THG experimental setup).

Upon pumping each MAST with our wavelength-tunable MOPA system, we routinely observe the intermodally phase-matched THG, as summarized in Fig. 4b–f. First, the field profile

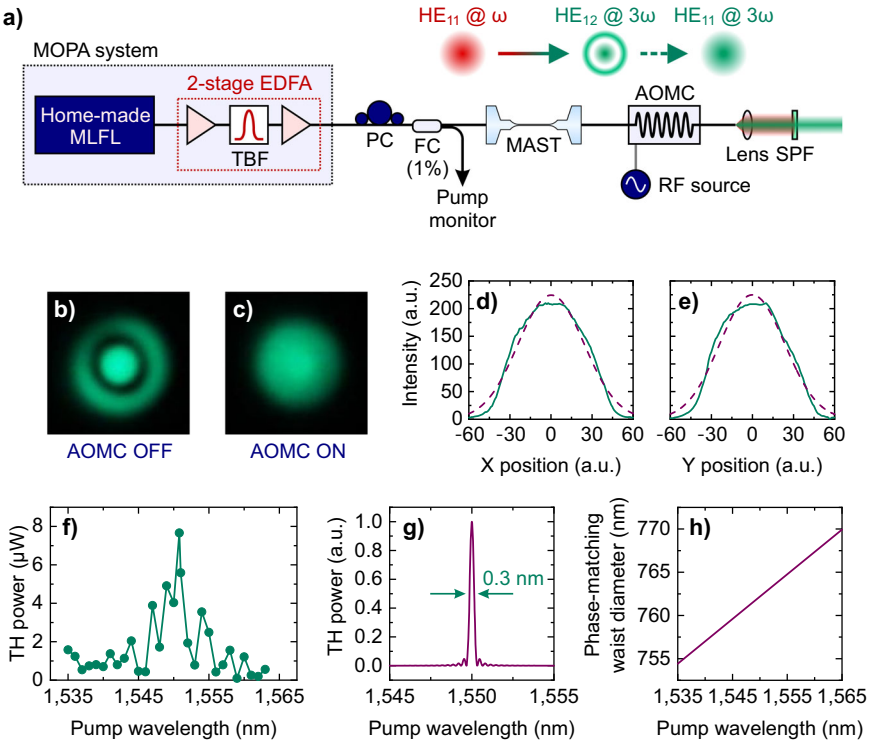

Fig. 4 Fundamental-to-fundamental all-fiber phase-matched third-harmonic generation in multimode adiabatic submicron tapers (MASTs). a Schematic diagram of the experimental setup. Red and turquoise in the beam path indicate the ~1550 nm pump beam and the third harmonic, respectively. The output pump beam is rejected at the short-pass filter (SPF), while the third-harmonic signal passes through the SPF and then characterized using a complementary metal-oxide-semiconductor (CMOS) camera, a power meter, and a grating-based optical spectrum analyzer. MOPA master oscillator power amplifier, MLFL mode-locked fiber laser, EDFA erbium-doped fiber amplifier, TBF tunable bandpass filter, PC polarization controller, FC fiber coupler, AOMC acousto-optic mode converter, RF radio frequency. **b**, **c** Measured far-field patterns of the output third-harmonic signal when the AOMC is turned off (**b**) and switched on (**c**). **d**, **e** Gaussian fits (purple dashed curves) to the experimentally obtained intensity profiles (turquoise solid curves) from **c**. **f** Third-harmonic (TH) output powers measured at an average pump power of 0.14 W over the entire tuning range of pump wavelength. In this case, the third-harmonic power peaks at a pump wavelength of 1550.80 nm, where the third-harmonic conversion efficiency is determined as 5.5×10^{-5} (third-harmonic power: 7.7 μW). Error bars (one standard deviation from the mean) are smaller than the data points. **g** Theoretically predicted third-harmonic power as a function of pump wavelength with an assumption of uniform waist diameter (0.76 μm). **h** Calculated phase-matching waist diameter as a function of pump wavelength.

of the LP_{02} mode of the output third-harmonic signal is clearly seen when the AOMC is switched off (Fig. 4b), thanks to the adiabatic transmission of the LP_{02} mode along the MAST. Furthermore, this third harmonic in the LP_{02} mode can be converted into the LP_{01} mode with high purity (Fig. 4c–e), as we turn on the AOMC. We emphasize that this not only further verifies the capability and benefit of adiabatic transmission of the LP_{02} mode of our MAST but also experimentally demonstrates the fundamental-to-fundamental THG in the waveguide platform. To show that the THG is phase-matched, we measure the third-harmonic output power while scanning the pump wavelength. The third-harmonic power peaks when the pump wavelength is tuned to 1550.80 nm, as shown in Fig. 4f, which is very close to the theoretically predicted phase-matching pump wavelength of 1550.0 nm for the experimentally measured waist diameter of 0.76 μm (Fig. 2c). It is noteworthy to mention that the third-harmonic signal is also weakly observed over the entire pump wavelength tuning range of the MOPA system (1535–1563 nm). Considering the theoretically anticipated THG bandwidth to be as narrow as 0.3 nm (Fig. 4g), we believe that such relatively broadband THG in experiments is due to the nonuniformity of MAST waist diameter. The phase-matching pump wavelength for the THG process is highly sensitive to the waist diameter[43], and our numerical calculation indicates that the variation of waist diameter of only 15 nm gives rise to the shift of phase-matching pump wavelength by an amount of the MOPA tuning range of 28 nm (Fig. 4h). The nonuniformity of the waist diameter is attributed to the imperfection of our current tapering facility in the submicron thickness regime that we mentioned previously. We note that the insufficient spatial resolution (5 nm) of the scanning electron microscope used in our experiment (Fig. 2c) hinders the precise measurement of such a small amount of nonuniformity of the waist diameter.

For further verification of the THG, we examine the dependence of the third-harmonic power on the pump power and pump polarization, as shown in Fig. 5a. The third-harmonic power is highly dependent on the pump polarization. When we keep adjusting the pump polarization to maximize the third-harmonic signal, the measured third-harmonic powers exhibit excellent agreement with the well-known cubic dependence on the pump power[28]. We achieve a maximum conversion efficiency of 1.5×10^{-4} (71 μW third-harmonic output power) at the pump power of 0.48 W. We also measure the pump power dependence of the third-harmonic power when the pump polarization is adjusted to suppress the THG as much as possible. At low pump powers, the third-harmonic power can be reduced by a factor of ~1/10, while also displaying a cubic dependence on the pump power. In isotropic media such as fused silica glass, the THG process via $\chi^{(3)}$ nonlinearity becomes most efficient for a linearly polarized pump beam, whereas it is eliminated when the pump

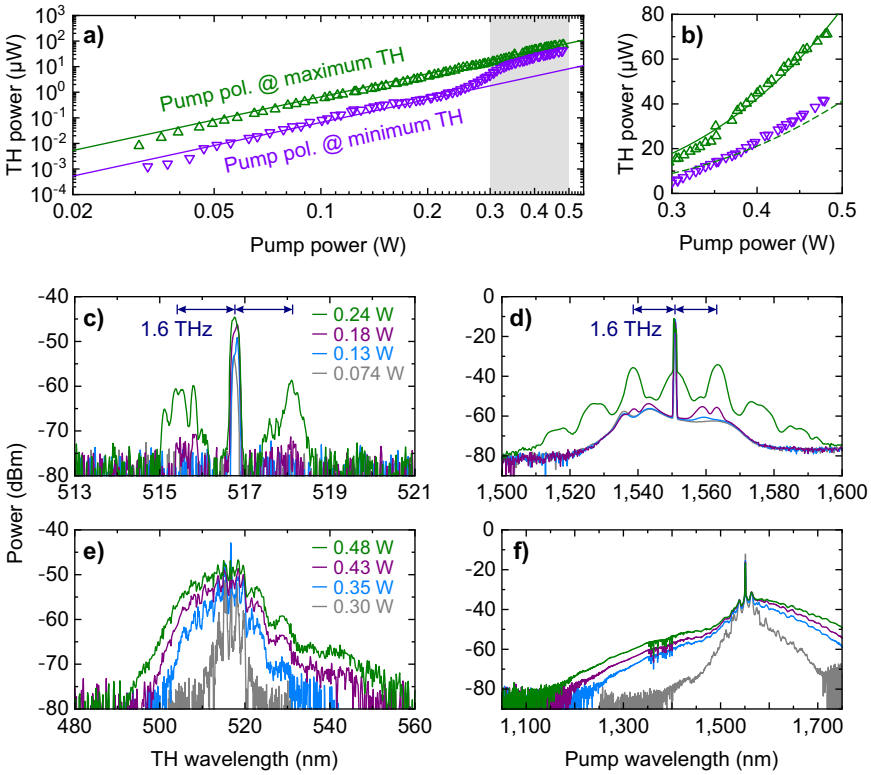

Fig. 5 Pump power dependence of third-harmonic generation. a Measured third-harmonic (TH) powers over a range of average pump power, while the input pump polarization (pol.) is adjusted to yield the maximum (green triangles) or minimum (violet triangles) third-harmonic power for each pump power. The green and violet lines are the cubic fits to the measured maximum and minimum third-harmonic powers, respectively. Error bars (one standard deviation from the mean) are smaller than the data points. **b** Zoomed-in plot around the gray region in (**a**). The green solid curve is the same as the cubit fit (green line) in (**a**), and the green dashed curve stands for half of the cubit fit. Error bars (one standard deviation from the mean) are smaller than the data points. Optical spectra of the third-harmonic signal (**c**) and output pump beam (**d**) at relatively low average pump powers (0.074, 0.13, 0.18, and 0.24 W). Optical spectra of the third-harmonic signal (**e**) and output pump beam (**f**) at relatively high average pump powers (0.30, 0.35, 0.43, and 0.48 W). Each color in (**d**) and (**f**) corresponds to the average pump power displayed in (**c**) and (**e**), respectively.

beam is circularly polarized[44]. This polarization property should also be exhibited in MASTs, where the third-harmonic signal is in the HE_{12} mode that has the same azimuthal dependence of the field distribution as the pump beam in the HE_{11} mode. The nonzero minimum third-harmonic signal observed in experiments is attributed to the residual birefringence in the MAST that can arise from slightly broken circular symmetry of the cross-section of the fabricated MAST we mentioned previously, which hinders the preservation of the circular polarization of the pump beam during its propagation along the MAST waist. On the other hand, as the pump power rises further, the THG becomes less polarization-sensitive, with an increase in the minimum third-harmonic conversion efficiency. The minimum third-harmonic conversion efficiency is locked to about half the maximum value at sufficiently high pump powers, as shown in Fig. 5b. Such unusual pump polarization dependence might arise from the complicated nonlinear polarization dynamics in the MAST waist[45], which we will investigate in detail in our future study.

Finally, we measure the optical spectrum of the third-harmonic signal, together with that of the output pump beam for comparison, as shown in Fig. 5c–f. At low pump powers (0.13 W), a narrowband third-harmonic signal is observed at 516.8 nm and increases as the pump power rises. When the pump power reaches 0.18 W, spectral sidebands are created on both sides at a distance of ~1.6 THz from the main third-harmonic peak. Such spectral sidebands also appear in the output pump spectrum with the same spectral distance (~1.6 THz). This indicates that the sidebands are first created in the pump beam via self-phase-modulation (SPM)-induced modulation instability during propagation along the single-mode lead fiber, and then the same sidebands are generated in the third-harmonic signal via cross-phase-modulation-induced modulation instability[46,47] in the MAST rather than the THG of the pump beam sidebands or the SPM-induced modulation instability arising from the main third-harmonic peak. We check that such spectral broadening of the pump beam does not appear when the MAST is replaced by intact optical fiber. When the pump power exceeds 0.3 W, both the pump beam and the third-harmonic signal experience significant asymmetric spectral broadening (Fig. 5e, f) that arises from nonlinear phase modulation[48].

Discussion

We compare the THG performance in this work with some representative previous ones in Table 1. We have achieved a single-pass THG conversion efficiency of 1.5×10^{-4} at an average pump power of 0.48 W in a MAST waist as short as 10 mm only. It should be noticed that this conversion efficiency is already higher than or comparable to those in relevant previous works, even though it is currently limited primarily by the relatively short MAST waist due to the technical issues in the fabrication of longer MASTs we mentioned previously. Since the THG conversion efficiency is proportional to the square of interaction length in the undepleted-pump regime[28], it may be worth comparing THG conversion efficiencies per square of waist length. We highlight that the unique capability of the MAST to transmit

Table 1 Comparison of the third-harmonic generation performance between this work and representative examples from the literature.

Ref. #	Pump wavelength (nm)	Peak pump power (kW)	Average pump power (W)	Waist length (mm)	Total conversion efficiency
This work	1550	1.9	0.48	10	1.5×10^{-4}
20	1250	10.7	0.45	90	5×10^{-4}
22	1550	1.25	0.5	45	3×10^{-4}
23	1550	1.5	0.06	50	2.5×10^{-7}
25	1091	2.6	1.2	6	4×10^{-7}

the LP_{02} mode adiabatically leads to a record-high THG conversion efficiency per square of waist length ($1.5\ m^{-2}$), which is markedly greater than those in any other previous works using nonadiabatic counterparts by one order of magnitude or larger.

We expect that the THG conversion efficiency can be further improved by increasing the waist length and the uniformity of the waist diameter or employing the cascaded scheme[49]. This waist length is currently limited by the taper being lifted up and curved in the tapering process under the influence of the butane–oxygen gas flow, which deteriorates the thickness uniformity of the taper waist. We observe that wet-etched fibers are more compliant to such gas-flow-induced deformation during the tapering process compared to the case of direct tapering of non-etched conventional optical fibers, which implies that the suppression of the effect of gas flow is essential in the production of high-quality MASTs. We expect that the use of a heat source that does not produce such gas flow, e.g., a focused carbon-dioxide laser beam[50] or an electric micro-heater[51], may resolve the issue and thus enable the fabrication of MASTs with a longer waist and higher transmission.

A technical consensus on the flame brushing and pulling technique is that it is practically challenging to precisely reproduce the targeted nanotaper waist using that tapering method[39]. In our experiments, we fabricate eight MAST samples and examine the adiabaticity of their LP_{02} mode transmission and THG characteristics to evaluate the reproducibility of our sample fabrication. We observe intermodally phase-matched THG for all the MAST samples with similar amounts of conversion efficiency via simple tuning of the pump laser wavelength within 1535–1560 nm. This experimental result implies that the waist diameters of the fabricated MASTs have deviations below ±10 nm (Fig. 4h), which is sufficiently small for the experiments using our wavelength-tunable pump laser source.

The unique capability of our MAST to adiabatically transmit several HOMs simultaneously, combined with our all-fiber devices that perform the near-unity-efficiency in-fiber mode conversion between the LP_{01} mode and the HOM (at least the LP_{11}, LP_{21}, and LP_{02} modes), offers a variety of intriguing opportunities in the emerging field of multimode nonlinear optics and quantum optics[52]. Novel multimode nonlinear optical frequency conversion[53,54] and nonclassical light generation[26,27,29], multimode photonic quantum information processing[55,56], and broadband spatiotemporal dynamics[57,58] can be investigated with high efficiencies in all-fiber platforms. Furthermore, manipulation of the evanescent field profiles can be facilitated through excitation of HOMs in the MAST waist for tailoring the optical trapping potentials of atoms and nanoparticles[59]. Our MAST can also improve the performance of taper-based photonic devices and implement new types of components for multimode optics experiments. For instance, when a saturable absorber or a two-dimensional nanomaterial is deposited on the MAST waist[60], its operating power can be significantly reduced by transmitting the HOM instead of the LP_{01} mode because of the larger evanescent field of the HOM.

Methods

Fabrication and in situ characterization of MASTs. We fabricate silica MASTs employing a two-step process, as described in Fig. 2a. A section of unjacketed conventional step-index silica optical fiber, single-mode fiber at telecom wavelength (~1550 nm) with the core diameter of 8.7 μm and the numerical aperture of 0.13 (manufacturer: LS Cable & System), is wet-etched using 6:1 buffered oxide etch solution to reduce the cladding diameter from 125 μm down to below ~20 μm (Fig. 2b). The LP_{11}, LP_{21}, and LP_{02} modes are the core modes at 532 nm wavelength (fiber V parameter: 6.7). The wet-etched fiber section is then tapered to a sub-micron thickness to produce a final MAST (Fig. 2c) via the flame brushing and pulling technique[36,37] using a butane–oxygen flame as a heat source. To check the adiabatic transmission of each optical mode during the tapering process, we monitor the transmission and far-field pattern simultaneously at the MAST output port, while a laser beam at 532 nm wavelength is coupled into each of the LP_{02}, LP_{21}, and LP_{11} modes of the MAST input port, as illustrated in Fig. 3a. To this end, the 532 nm laser beam emitted from a diode-pumped solid-state laser is launched primarily into the LP_{01} mode of the fiber, and the remnant HOMs are removed using a taper-based mode stripper[61] to obtain the pure LP_{01} mode. The LP_{01} mode is then converted into a target HOM using a home-made all-fiber acousto-optic mode converter (AOMC)[41,42] or a microbend-induced long-period fiber grating[62], whose conversion efficiencies are measured to be as high as ~96% and ~98%, respectively. The transmission and output far-field pattern are recorded for each input HOM using a power meter and a CMOS camera, respectively, during the entire tapering process.

Observation of fundamental-to-fundamental all-fiber THG in silica MASTs. Figure 4a illustrates our experimental scheme of fundamental-to-fundamental all-fiber THG. A fabricated MAST is first packaged in an acrylic box for long-term protection from contamination with dust and moisture as well as other environmental perturbations, which is crucial for the practical use of MASTs. The MAST is pumped by optical pulses generated from a MOPA system that utilizes our widely tunable ultra-narrow-linewidth dissipative soliton erbium-doped fiber laser[40] as the oscillator. The soliton fiber laser emits an 8 GHz (64 pm)-linewidth, 110 ps-width pulse train at a repetition rate of 2.1 MHz, whose optical wavelength can be tuned over a wide range (1530–1563 nm). The output of the seed laser is amplified using a two-stage erbium-doped fiber amplifier (EDFA) consisting of a home-made pre-amplifier and a power amplifier. A tunable bandpass filter (TBF) having a bandwidth of 0.8 nm is inserted between the two amplifiers to suppress the amplified spontaneous emission noise from the amplifiers, where the center wavelength of the TBF is adjusted according to the laser wavelength. The pulse width of the MOPA output is measured to be 110 ps by using an intensity autocorrelator. We emphasize that the 110 ps pulse width is sufficiently broad compared to the theoretically predicted temporal walk-off of 8 ps between the fundamental wave in the HE_{11} mode and the third harmonic in the HE_{12} mode in the 10 mm-long MAST waist, allowing their temporal overlap to be maintained significantly over the entire MAST waist (see Supplementary Note 2 and Supplementary Fig. 3). We note that due to the insufficient spectral response of our EDFA at shorter wavelengths, the resultant wavelength tuning range of our MOPA is slightly reduced to 1535–1563 nm. In addition, the maximally attainable pulse peak power for the THG experiments is 1.9 kW, which is mainly limited by the nonlinear spectral broadening at the power amplifier in the two-stage EDFA (see Supplementary Note 2 and Supplementary Fig. 3). A fiber polarization controller is used after the EDFA to adjust the polarization state of the pump beam for the examination of the pump polarization dependence of the THG process. A 1% fiber tapping coupler is inserted right before the MAST to monitor the pump power. The pump beam is partly converted into the third harmonic in the HE_{12} mode in the MAST, which is then transformed into the desired LP_{01} mode at a home-made all-fiber AOMC[41,42] right after the MAST. Before the THG experiments, we check that a nearly complete (~95%) acousto-optic intermodal conversion is achieved at the AOMC between the LP_{01} and the LP_{02} mode at ~517 nm wavelength when a sinusoidal electric signal of 23 $V_{p\text{-}p}$ at 1.404 MHz is applied to the acoustic transducer of the AOMC. The remaining pump beam is rejected right after the fiber output using a short-pass filter. The optical power, far-field pattern, and optical spectrum of the output third-harmonic signal are measured with a power meter, a CMOS camera, and a grating-based optical spectrum analyzer, respectively.

Data availability

The data that support the findings of this study are available from the corresponding author upon reasonable request.

Code availability

The custom codes are available from the corresponding author upon reasonable request.

Received: 12 October 2020; Accepted: 15 July 2021;
Published online: 02 August 2021

References

1. Tong, L. et al. Subwavelength-diameter silica wires for low-loss optical wave guiding. *Nature* **426**, 816–819 (2003).
2. Brambilla, G., Finazzi, V. & Richardson, D. J. Ultra-low-loss optical fiber nanotapers. *Opt. Express* **12**, 2258–2263 (2004).
3. Cai, M., Painter, O. & Vahala, K. J. Observation of critical coupling in a fiber taper to a silica-microsphere whispering-gallery mode system. *Phys. Rev. Lett.* **85**, 74–77 (2000).
4. Spillane, S. M., Kippenberg, T. J., Painter, O. J. & Vahala, K. J. Ideality in a fiber-taper-coupled microresonator system for application to cavity quantum electrodynamics. *Phys. Rev. Lett.* **91**, 043902 (2003).
5. Fujiwara, M., Toubaru, K., Noda, T., Zhao, H.-Q. & Takeuchi, S. Highly efficient coupling of photons from nanoemitters into single-mode optical fibers. *Nano Lett.* **11**, 4362–4365 (2011).
6. Yalla, R., Kien, F. L., Morinaga, M. & Hakuta, K. Efficient channeling of fluorescence photons from single quantum dots into guided modes of optical nanofiber. *Phys. Rev. Lett.* **109**, 063602 (2012).
7. Vetsch, E. et al. Optical interface created by laser-cooled atoms trapped in the evanescent field surrounding an optical nanofiber. *Phys. Rev. Lett.* **104**, 203603 (2010).
8. Gouraud, B., Maxein, D., Nicolas, A., Morin, O. & Laurat, J. Demonstration of a memory for tightly guided light in an optical nanofiber. *Phys. Rev. Lett.* **114**, 180503 (2015).
9. Kato, S. & Aoki, T. Strong coupling between a trapped single atom and an all-fiber cavity. *Phys. Rev. Lett.* **115**, 093603 (2015).
10. Sørensen, H. L. et al. Coherent backscattering of light off one-dimensional atomic strings. *Phys. Rev. Lett.* **117**, 133604 (2016).
11. Petersen, J., Volz, J. & Rauschenbeutel, A. Chiral nanophotonic waveguide interface based on spin-orbit interaction of light. *Science* **346**, 67–71 (2014).
12. Daly, M., Truong, V. G. & Nic Chormaic, S. Evanescent field trapping of nanoparticles using nanostructured ultrathin optical fibers. *Opt. Express* **24**, 14470–14482 (2016).
13. Jin, W., Ho, H. L., Cao, Y. C., Ju, J. & Qi, L. F. Gas detection with micro- and nano-engineered optical fibers. *Opt. Fiber Technol.* **19**, 741–759 (2013).
14. Ding, Z. et al. Distributed refractive index sensing based on tapered fibers in optical frequency domain reflectometry. *Opt. Express* **26**, 13042–13054 (2018).
15. Leon-Saval, S. G., Birks, T. A., Wadsworth, W. J., Russell, P. St. J. & Mason, M. W. Supercontinuum generation in submicron fibre waveguides. *Opt. Express* **12**, 2864–2869 (2004).
16. Kang, M. S., Brenn, A., Wiederhecker, G. S. & Russell, P. St. J. Optical excitation and characterization of gigahertz acoustic resonances in optical fiber tapers. *Appl. Phys. Lett.* **93**, 131110 (2008).
17. Beugnot, J.-C. et al. Brillouin light scattering from surface acoustic waves in a subwavelength-diameter optical fibre. *Nat. Commun.* **5**, 5242 (2014).
18. Cui, L. et al. Generation of correlated photon pairs in micro/nano-fibers. *Opt. Lett.* **38**, 5063–5066 (2013).
19. Kim, J., Ihn, Y. S., Kim, Y. & Shin, H. Photon-pair source working in a silicon-based detector wavelength range using tapered micro/nanofibers. *Opt. Lett.* **44**, 447–450 (2019).
20. Akimov, D. A. et al. Generation of a spectrally asymmetric third harmonic with unamplified 30-fs Cr:forsterite laser pulses in a tapered fiber. *Appl. Phys. B* **76**, 515–519 (2003).
21. Grubsky, V. & Feinberg, J. Phase-matched third-harmonic UV generation using low-order modes in a glass micro-fiber. *Opt. Commun.* **274**, 447–450 (2007).
22. Lee, T. et al. Broadband third harmonic generation in tapered silica fibres. *Opt. Express* **20**, 8503–8511 (2012).
23. Coillet, A. & Grelu, P. Third-harmonic generation in optical microfibers: from silica experiments to highly nonlinear glass prospects. *Opt. Commun.* **285**, 3493–3497 (2012).
24. Gouveia, M. A. et al. Second harmonic generation and enhancement in microfibers and loop resonators. *Appl. Phys. Lett.* **102**, 201120 (2013).
25. Jiang, X. et al. Enhanced UV third-harmonic generation in microfibers by controlling nonlinear phase modulations. *Opt. Lett.* **44**, 4191–4194 (2019).
26. Corona, M., Garay-Palmett, K. & U'Ren, A. B. Third-order spontaneous parametric down-conversion in thin optical fibers as a photon-triplet source. *Phys. Rev. A* **84**, 033823 (2011).
27. Dot, A., Borne, A., Boulanger, B., Bencheikh, K. & Levenson, J. A. Quantum theory analysis of triple photons generated by a $\chi^{(3)}$ process. *Phys. Rev. A* **85**, 023809 (2012).
28. Grubsky, V. & Savchenko, A. Glass micro-fibers for efficient third harmonic generation. *Opt. Express* **13**, 6798–6806 (2005).
29. Signorini, S. et al. Intermodal four-wave mixing in silicon waveguides. *Photon. Res.* **6**, 805–814 (2018).
30. Mishra, V., Singh, S. P., Haldar, R., Mondal, P. & Varshney, S. K. Intermodal nonlinear effects mediated optical event horizon in short-length multimode fiber. *Phys. Rev. A* **96**, 013807 (2017).
31. Rishøj, L., Tai, B., Kristensen, P. & Ramachandran, S. Soliton self-mode conversion: revisiting Raman scattering of ultrashort pulses. *Optica* **6**, 304–308 (2019).
32. Ravets, S. et al. A low-loss photonic silica nanofiber for higher-order modes. *Opt. Express* **21**, 18325–18335 (2013).
33. Ward, J. M., Maimaiti, A., Le, V. H. & Nic Chormaic, S. Optical micro- and nanofiber pulling rig. *Rev. Sci. Instrum.* **85**, 111501 (2014).
34. Harrington, K., Yerolatsitis, S., Ras, D. V., Haynes, D. M. & Birks, T. A. Endlessly adiabatic fiber with a logarithmic refractive index distribution. *Optica* **4**, 1526–1533 (2017).
35. Jung, Y., Harrington, K., Yerolatsitis, S., Richardson, D. J. & Birks, T. A. Adiabatic higher-order mode microfibers based on a logarithmic index profile. *Opt. Express* **28**, 19126–19132 (2020).
36. Jiang, X., Lee, T., He, J., Abdul Khudus, M. I. M. & Brambilla, G. Fundamental-mode third harmonic generation in microfibers by pulse-induced quasi-phase matching. *Opt. Express* **25**, 22626–22639 (2017).
37. Birks, T. A. & Li, Y. W. The shape of fiber tapers. *J. Light. Technol.* **10**, 432–438 (1992).
38. Love, J. D. et al. Tapered single-mode fibres and devices. I. adiabaticity criteria. *IEEE Proc. J. Optoelectron.* **138**, 343–354 (1991).
39. Xu, Y., Fang, W. & Tong, L. Real-time control of micro/nanofiber waist diameter with ultrahigh accuracy and precision. *Opt. Express* **25**, 10434–10440 (2017).
40. Ha, C. K., Lee, K. S., Kwon, D. & Kang, M. S. Widely tunable ultra-narrow-linewidth dissipative soliton generation at telecom band. *Photon. Res.* **8**, 1100–1109 (2020).
41. Zhao, J. & Liu, X. Fiber acousto-optic mode coupling between the higher-order modes with adjacent azimuthal numbers. *Opt. Lett.* **31**, 1609–1611 (2006).
42. Zhao, J., Miao, R. & Liu, X. Nonresonant cascaded acousto-optic mode coupling. *Opt. Lett.* **31**, 2909–2911 (2006).
43. Abdul Khudus, M. I. M., Lee, T., Horak, P. & Brambilla, G. Effect of intrinsic surface roughness on the efficiency of intermodal phase matching in silica optical nanofibers. *Opt. Lett.* **40**, 1318–1321 (2015).
44. Bey, P. P., Giuliani, J. H. & Rabin, H. Linear and circular polarized laser radiation in optical third harmonic generation. *Phys. Lett.* **26A**, 128–129 (1968).
45. Hartley, D., Lohe, M. A., Monro, T. M. & Afshar V., S. Cross mode and polarization mixing in third and one-third harmonic generation in multimode waveguides. *J. Opt. Soc. Am. B* **32**, 379–387 (2015).
46. Agrawal, G. P. Modulation instability induced by cross-phase modulation. *Phys. Rev. Lett.* **59**, 880–883 (1987).
47. Band, Y. B. Phase-modulation effects on the spectrum of third-harmonic generation. *Phys. Rev. A* **42**, 5530–5536 (1990).
48. Naumov, A. N. & Zheltikov, A. M. Asymmetric spectral broadening and temporal evolution of cross-phase-modulated third-harmonic pulses. *Opt. Express* **10**, 122–127 (2002).
49. Jiang, X., Chen, Z., Lee, T. & Brambilla, G. Coherently enhanced third-harmonic generation in cascaded microfibers. *Opt. Lett.* **45**, 3272–3275 (2020).
50. Yokota, H., Sugai, E. & Sasaki, Y. Optical irradiation method for fiber coupler fabrications. *Opt. Rev.* **4**, 104–107 (1997).
51. Ding, L., Belacel, C., Ducci, S., Leo, G. & Favero, I. Ultralow loss single-mode silica tapers manufactured by a microheater. *Appl. Opt.* **49**, 2441–2445 (2010).
52. Krupa, K. et al. Multimode nonlinear fiber optics, a spatiotemporal avenue. *APL Photon.* **4**, 110901 (2019).
53. Chen, Y., Chen, Z., Wadsworth, W. J. & Birks, T. A. Nonlinear optics in the LP_{02} higher-order mode of a fiber. *Opt. Express* **21**, 17786–17799 (2013).
54. Demas, J., Rishøj, L., Liu, X., Prabhakar, G. & Ramachandran, S. Intermodal group-velocity engineering for broadband nonlinear optics. *Photon. Res.* **7**, 1–7 (2019).
55. Feng, L.-T. et al. On-chip coherent conversion of photonic quantum entanglement between different degrees of freedom. *Nat. Commun.* **7**, 11985 (2016).
56. Feng, L.-T. et al. On-chip transverse-mode entangled photon pair source. *NPJ Quantum Inf.* **5**, 2 (2019).

57. Wright, L. G., Christodoulides, D. N. & Wise, F. W. Spatiotemporal mode-locking in multimode fiber lasers. *Science* **358**, 94–97 (2017).
58. Wright, L. G. et al. Mechanisms of spatiotemporal mode-locking. *Nat. Phys.* **16**, 565–570 (2020).
59. Maimaiti, A., Truong, V. G., Sergides, M., Gusachenko, I. & Nic Chormaic, S. Higher order microfiber modes for dielectric particle trapping and propulsion. *Sci. Rep.* **5**, 9077 (2015).
60. Martinez, A. et al. Low-loss saturable absorbers based on tapered fibers embedded in carbon nanotube/polymer composites. *APL Photon.* **2**, 126103 (2017).
61. Đonlagic, D. In-line higher order mode filters based on long highly uniform fiber tapers. *J. Light. Technol.* **24**, 3532–3539 (2006).
62. Blake, J. N., Kim, B. Y. & Shaw, H. J. Fiber-optic modal coupler using periodic microbending. *Opt. Lett.* **11**, 177–179 (1986).

Acknowledgements

This work was supported by the National Research Foundation of Korea (NRF) grants funded by the Korea government (MSIT) (NRF-2019R1A2C2088839).

Author contributions

M.S.K. conceived and supervised the work. All authors constructed the fiber tapering facility, and C.K.H. and K.H.N. fabricated MAST samples. C.K.H. constructed the measurement setup and performed the measurements and numerical calculations. C.K.H. and M.S.K. analyzed the experimental and theoretical data. All authors had discussions, and C. K.H. and M.S.K. wrote the manuscript.

Competing interests

The authors declare no competing interests.

Additional information

Supplementary information The online version contains supplementary material available at https://doi.org/10.1038/s42005-021-00677-2.

Correspondence and requests for materials should be addressed to M.S.K.

Peer review information *Communications Physics* thanks Xunsi Wang, [name] and the other, anonymous, reviewer(s) for their contribution to the peer review of this work. Peer reviewer reports are available.

Reprints and permission information is available at http://www.nature.com/reprints

Publisher's note Springer Nature remains neutral with regard to jurisdictional claims in published maps and institutional affiliations.